On the Nature of Freestream Disturbances in a Two-Dimensional Supersonic Test Section

Chitrarth Prasad *, Junji Huang †, Lian Duan ‡ and Datta Gaitonde §
The Ohio State University, Columbus, Ohio 43210

Conventional wind tunnels are often prone to elevated levels of freestream disturbances than those actually encountered in flight. This limits their applicability in ground-tests where the laminar-turbulent transition plays an important role. The goal of the present investigation is to obtain an improved understanding of noise radiation from supersonic boundary layers in a geometrically confined environment. To this end, the fluctuations in a well-validated Mach 2.5 rectangular channel DNS database are decomposed into their constituent solenoidal, acoustic and thermal fluid thermodynamic (FT) components. This decomposition provides substantial insight into the observed radiating and non-radiating parts of the flow. However, it does not by itself identify the local mechanisms responsible for noise generation in wall boundary layers. To address this, the Navier-Stokes equations are rewritten as an exact, inhomogeneous, convected wave equation, which governs the generation and propagation of fluctuating stagnation enthalpy (FSE) from the wall boundary layers to the core of the channel. It is shown that the FSE is a scaled surrogate for pressure fluctuations away from the wall boundary layers and can be decomposed into its own solenoidal, acoustic and thermal FT components. Thus, sources terms in the FSE wave equation provide an improved understanding of the local mechanisms responsible for noise radiation from the wall boundary layers. A careful inspection of the instantaneous distributions of both FSE sources and FT components identifies the most acoustically relevant mechanism in the wall boundary layers.

Nomenclature

H	=	shape factor, $H = \delta^*/\theta$, dimensionless
(L_x, L_y, L_z)	=	Computational domain size along (x, y, z) directions, m
M	=	Mach number, dimensionless
Pr	=	Prandtl number, $Pr = 0.71$, dimensionless
P_∞	=	freestream mean pressure, Pa
R	=	ideal gas constant, $R = 287$, J/(K·kg)
Re_θ	=	Reynolds number based on momentum thickness and freestream viscosity, $Re_\theta = \rho_\infty U_\infty \theta/\mu_\infty$, dimensionless
$Re_{\delta 2}$	=	Reynolds number based on momentum thickness and wall viscosity, $Re_{\delta 2} = \rho_\infty U_\infty \theta/\mu_w$, dimensionless
Re_τ	=	Reynolds number based on shear velocity and wall viscosity, $Re_\tau = \rho_w U_\infty \delta/\mu_w$, dimensionless
T	=	temperature, K
T_r	=	recovery temperature, $T_r = T_\infty(1 + 0.89\frac{\gamma-1}{2}M_\infty^2)$
U_∞	=	freestream velocity, m/s
p	=	pressure, Pa
u	=	streamwise velocity, m/s
u_τ	=	friction velocity, m/s
v	=	spanwise velocity, m/s
w	=	wall-normal velocity, m/s
x	=	streamwise direction of the right-hand Cartesian coordinate
y	=	spanwise direction of the right-hand Cartesian coordinate
z	=	wall-normal direction of the right-hand Cartesian coordinate
Δx	=	streamwise separation used to evaluate spatial correlations
Δy	=	spanwise separation in spanwise direction

*Postdoctoral Researcher, Mechanical and Aerospace Engineering, AIAA Member
†Graduate Assistant, AIAA Student Member
‡Associate Professor, Aerospace Engineering, Senior AIAA Member
§Professor, Aerospace Engineering, AIAA Fellow

Δt = time delay
z_τ = viscous length, $z_\tau = \nu_w/u_\tau$, m
β = Clauser pressure-gradient parameter, $\beta = \delta^*/\tau_w dP_\infty/dx$, dimensionless
γ = specific heat ratio, dimensionless
δ = boundary layer thickness, m
δ^* = displacement thickness, m
θ = momentum thickness, m
κ = thermal conductivity, $\kappa = \mu C_p/Pr$, W/(m·K)
μ = dynamic viscosity, $\mu = 1.458 \times 10^{-6} \frac{T^{3/2}}{T+110.4}$, kg/(m·s)
ν = kinematic viscosity, $\nu = \mu/\rho$, m^2·s
ρ = density, kg/m^3
$\boldsymbol{\omega}$ = vorticity, s^{-1}
λ = expansion angle, deg
$\boldsymbol{B}$ = Hydrodynamic FT component of $\rho\boldsymbol{u}$
ψ' = Irrotational Scalar Potential
ψ'_a = Acoustic Scalar Potential
ψ'_t = Thermal Scalar Potential
S = Entropy
H' = Fluctuating Stagnation Enthalpy
H'_A = Acoustic Fluctuating Stagnation Enthalpy
H'_B = Hydrodynamic Fluctuating Stagnation Enthalpy
H'_T = Thermal Fluctuating Stagnation Enthalpy
$\boldsymbol{\alpha_1}$ = Coriolis Acceleration
$\boldsymbol{\alpha_2}$ = Acceleration due to shear and entropy gradients

Subscripts

i = inflow station for the domain of direct numerical simulations
rms = root mean square
w = wall variables
∞ = freestream variables
t = stagnation quantities

Superscripts

$+$ = inner wall units
$\overline{(\cdot)}$ = averaged variables
$(\cdot)'$ = perturbation from averaged variable

I. Introduction

A comprehensive understanding of the freestream disturbances from conventional high-speed wind tunnels can allow a more accurate extrapolation of the wind-tunnel data to flight. Several studies document the elevated freestream disturbance levels in conventional high-speed wind tunnels and their effect on flight testing [1–3]. This has led to various DNS studies to investigate the freestream disturbances from these tunnels. These studies primarily focus on the radiation from spatially developing turbulent boundary layers (TBLs) over flat plates [4–6]. They collectively include the effect of different freestream Mach numbers ranging from 2.5 to 14 both with and without wall cooling. The simpler geometry of flat plates allows an easier isolation of the acoustic radiation from a single surface based on different flow conditions and boundary layer parameters. Furthermore, DNS studies from axisymmetric nozzles [7] and rectangular wind tunnels [8, 9] have shown that the radiation intensity from a flat plate boundary layer can be superimposed at the core region of the test-section by multiplying with the number of radiation boundary layers following Laufer's observations [1]. An overview of these studies can be found in [10].

Although previous DNS studies have been successful in exploring the radiation characteristics of TBLs from different test-sections, they typically involve the use of spectral methods and correlations on pressure data to characterize the freestream acoustic disturbances. It is well known that the pressure field contains contributions due to both hydrodynamic and acoustic components [11]. This suggests that the use of a more physics-based decomposition of the flow-field into its constituent hydrodynamic and acoustic components can provide additional insights into the generation of freestream disturbances. The goal of the present investigation is to address this gap by applying Doak's Momentum Potential Theory (MPT) [12] to a well-validated DNS database of a double-wall (channel) configuration with two independent, spatially evolving flat-plate TBLs with an edge Mach number of $M_\infty = 2.5$ (Section II), similar

to that studied by Duan *et al.* [4] for the single flat-wall configuration. The application of MPT to the interior flow-field in a channel provides insights into the noise generation mechanisms in a geometrically confined environment. The study represents a first step toward understanding of the genesis of freestream disturbances in the context of actual wind-tunnel experiments and providing guidance for measuring and controlling tunnel disturbances in high-speed facilities.

Doak's MPT involves a Helmholtz decomposition of the momentum density flow-field ($\rho\boldsymbol{u}$) into its solenoidal and irrotational components. The irrotational component can be further split into acoustic and thermal components. This decomposition when used in conjunction with the principle of mass or momentum conservation and the equation of state, yields a pair of Poisson equations that can be used to effectively separate the radiating and non-radiating components of the flow at any time instant. Within the framework of Doak's MPT, these individual components are called Fluid-Thermodynamic (FT) components. Due to its robustness, this method has been used extensively to study the noise generation mechanisms in both subsonic and supersonic jets [13–15], to analyze the noise reduction concepts for military aircraft [16, 17] and to study hypersonic boundary layers [18] among others. The application of Doak's MPT to the present DNS database is documented in Section III of this paper.

The FT components obtained by independently solving their respective equations do not however contain any details of their sources or sinks. The present investigation attempts to explain the origin of the FT components by considering the fluctuating stagnation enthalpy (FSE) generation at the wall boundary layers. Unlike traditional acoustic analogies, which represent the physical processes of sound generation and propagation using the concept of equivalent sources in a fictitious medium, the FSE of a fluid satisfies an exact, inhomogeneous convected wave equation that explicitly contains terms representing the relevant local processes responsible for sound generation and propagation in a physically meaningful manner [19]. Furthermore, the FSE of a fluid can be decomposed into its constituent radiating and non-radiating components by an extension of the original MPT procedure [20]. This suggests that a detailed inspection of the individual terms of this FSE wave equation, coupled with Doak's MPT, can provide an improved understanding of the local mechanisms responsible for the generation and propagation of sound from the wall boundary layers. An inspection of these source terms along with further details on the FSE wave equation is presented in Section IV. Section V summarizes the present study and lays the groundwork for future efforts.

II. Mach 2.5 DNS database

The DNS database used in the present investigation corresponds to a spatially evolving Mach 2.5 channel flow. The channel has a slightly increasing height with an expansion angle of 0.3° to account for the boundary layer growth in the downstream direction. This expansion angle corresponds to a Clauser pressure-gradient parameter, $\beta \leq 0.05$. This low value of β indicates that the effect of pressure gradient on the wall boundary layers is insignificant [21]. The freestream and wall-temperature conditions are listed in Table 1.

M_∞	U_∞[m/s]	ρ_∞[kg/m^3]	T_∞[K]	T_w[K]
2.5	823.6	0.1	270.0	568.0

Table 1: Freestream conditions for the Mach 2.5 DNS database used in the present study

The database was generated by solving the full three-dimensional compressible Navier-Stokes equations. The working fluid is assumed as perfect gas. The components of the viscous stress tensor are obtained from the Newtonian fluid model, and the heat flux terms are linearly related to the temperature gradient through Fourier's law. The viscosity μ is calculated by Sutherland's law, and the thermal conductivity κ is computed from $\kappa = \mu C_p/Pr$, where $Pr = 0.71$ is the molecular Prandtl number. The convective terms are cast in a split form and discretized using a sixth-order accurate central scheme [22–24], whereas a fourth-order central difference scheme is used for both the first and second derivatives in viscous terms. The time integration is performed using a third-order low-storage Runge-Kutta scheme [25].

Two different configurations, an unbounded single-wall and a geometrically confined double-wall, are used in the present study. Two independent, spatially developing single-wall boundary layers are simulated using the well established recycling/rescaling turbulence inflow generation method [4,26]. To prevent the nonphysical low-frequency correlations being introduced by recycling procedure, a dynamic spanwise shifting is added following the procedure laid out by Morgan *et al.* [27]. Time series profiles are then extracted from these single-wall simulations and imposed as the inflow boundary conditions for the double-wall case. The wall-normal velocity component is allowed to decay to zero outside of boundary layer $z/\delta_i = 1.85$ up to channel center plane.

Figure 1 shows the computational setup for DNS of both the single-wall and double-wall cases. It should be noted that the double-wall case starts at $x_s/\delta_i = 12.5$. As stated earlier, both the bottom and top walls are kept open at a

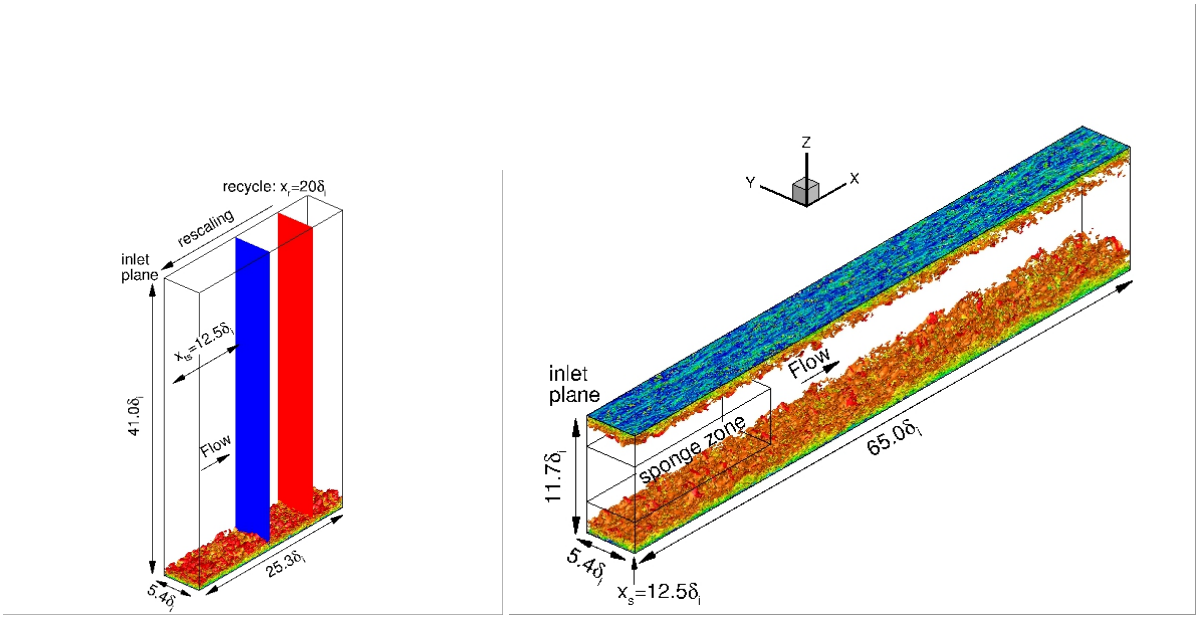

(a) (b)

Figure 1: Computational domain set up for the DNS case (a) Single Wall, and (b) Double Wall. The reference length δ_i is the inflow boundary layer thickness of case Single Wall. An instantaneous flow is shown in the domain visualized by iso-surface of the magnitude of density gradient, $|\Delta\rho|\delta_i/\rho_\infty = 0.98$, colored by the streamwise velocity component. x, y, and z are the streamwise, spanwise, and wall-normal coordinate, respectively. x_{ts} is the streamwise location where time series data of Single Wall are extracted. The black edge box near the Double Wall inflow region represents the sponge zone, which extends from $0 \le x/\delta_i \le 30.2$ in the streamwise direction, and $3.0 \le z/\delta_i < 8.7$ in the wall-normal direction.

fixed angle of $\lambda \approx 0.3^o$ with respect to the channel center plane. The domain size for the double-wall simulations is $(65.0\delta_i, 5.4\delta_i, 11.7\delta_i)$ in the streamwise (x), spanwise (y), and wall-normal (z) directions, where $\delta_i \approx 4.0$ mm is the inflow boundary layer thickness for the single-wall. The number of grid points in the streamwise, spanwise, and wall-normal directions are $(1960, 276, 581)$. The grid distribution is uniform in the streamwise and spanwise directions, with grid spacing of $\Delta x^+ = 8.9$ and $\Delta y^+ = 5.2$, respectively. In the wall-normal direction, the grid is clustered near bottom wall with $\Delta z^+ = 0.6$, and kept uniform with $\Delta z^+ = 9.0$ outside of the boundary layer all the way up to the channel center plane. The grid distribution in is symmetric about the channel center plane. A detailed list of the geometrical and mesh parameters is provided in Table 2. The inflow treatment mentioned above, is known to introduce a weak shock wave at the inflow station. To prevent the artificial inflow shock from interacting with the boundary layer along the opposite wall, a sponge zone is imposed near the center of the double-wall configuration. The sponge zone is imposed near the inflow at $0 \le (x - x_s)/\delta_i \le 17.7$ and $3.0 \le z/\delta_i \le 8.7$, by by adding a restoring body force vector, $\sigma(\mathbf{x})(q - q_{ref})$ to the governing equations [28]. The sponge strength parameter, σ is a function of x and z only and takes the form

$$\sigma(x, z) = a\left(1.0 - \frac{|z - z_c|}{h_s}\right)^2, \tag{1}$$

where z_c is the center plane height, and $h_s = 6.7\delta_i$ is the length of the sponge region in wall-normal direction. The constant a is set to $U_\infty/2\delta_i$, which is found to provide a gentle damping of the shock wave over the current sponge region. Figure 2 shows the instantaneous pressure field without and with inflow sponge. The pressure field, without inflow sponge, clearly indicates the inflow induced shock and its reflections from both walls in the downstream region. However, the strength of this shock system is relatively weak, with a mean pressure jump of about 2% in the channel center. With the use of inflow sponge, a significant reduction of the inflow induced shock is seen in Figure 2b. The mean pressure jump is reduced to about 0.5% with the current sponge strength. Figure 3 shows the acoustic radiation using numerical schlieren of density gradient, and it furthur shows that the inflow induced shock is faded out by the inflow sponge, while not affecting the downstream acoustic field or the boundary layer.

A no-slip condition is applied for all the three velocity components at the wall. The wall temperature is kept constant at T_w = 568 K, which is approximately the adiabatic wall temperature. An unsteady non-reflecting boundary condition [29] is imposed at the outlet boundary, whereas periodic boundary conditions are applied in the spanwise direction.

Table 3 lists the value of the boundary layer parameters at the reference location ($x_a = 46.3\delta_i$), including the momentum thickness θ, shape factor $H = \delta^*/\theta$, boundary layer thickness δ, viscous length z_τ, friction velocity u_τ, and three different Reynolds number parameters, Re_θ, Re_τ, and $Re_{\delta 2}$. The values are comparable to those from the previous DNS data [4]. Figure 4(a) compares the van Driest transformed mean velocity profile plotted in inner scale z^+ with the previously published data from a single wall turbulent boundary layer [4]. The velocity profile for the double-wall case is observed to be in excellent agreement with the previously published data. The root mean square (r.m.s.) pressure fluctuations are plotted in figure 4(b) in outer scale z/δ. Within the boundary layer, the pressure fluctuations nearly collapse on the single-wall data [4]. In the free stream, the level of pressure fluctuation for the double-wall is about 0.55, which is higher than the single-wall pressure fluctuation value of 0.4. This corresponds to a freestream pressure fluctuation ratio, $\left(p'_{rms}\right)_{DoubleWall} / \left(p'_{rms}\right)_{SingleWall} \approx \sqrt{2}$ for the two cases. This indicates that the intensity of the freestream pressure fluctuations for double-wall case is nearly 2 times that of the single-wall case. This finding is consistent with the observations by Laufer [1], who reported that the acoustic fluctuations radiated from multiple tunnel walls can be superimposed in a mean-square sense and, hence, that the intensity of pressure fluctuations in the core region of the tunnel test section is approximately equal to that radiated from a single tunnel-wall boundary layer multiplied by the number of radiating walls. An analogous result for a Mach 6 test section is also available in literature [8, 9]. These comparisons provide confidence in the use of the double-wall DNS database for the present work.

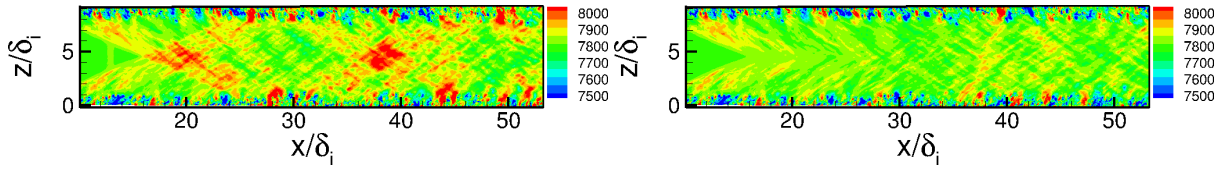

Figure 2: Instantaneous pressure contour for the case (*a*) M2.5 double wall without sponge; (*b*) M2.5 double wall with inlet sponge.

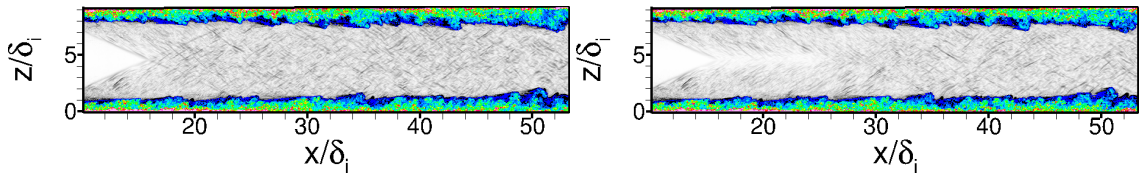

Figure 3: Instantaneous flow visualization for the case (*a*) M2.5 double wall without sponge; (*b*) M2.5 double wall with inlet sponge. The grey contours represent the density gradient, and the colour contours are the magnitude of vorticity, with contour level selected to emphasize the large-scale motions within the boundary layer.

Table 2: Grid resolution and domain size for the DNS with δ_i = 4.0 mm, z_τ = 0.015 mm.

Case	L_x/δ_i	L_y/δ_i	L_z/δ_i	$N_x \times N_y \times N_z$	Δx^+	Δy^+	Δz^+_{min}	Δz^+_{max}
Single Wall (×2)	25.3	5.4	41.0	$780 \times 276 \times 574$	8.9	5.2	0.6	8.7
Double Wall	65.0	5.4	11.7	$1960 \times 276 \times 581$	8.9	5.2	0.6	9.0

Table 3: Boundary layer properties at the station x_a selected for the statistical analysis.

Case	x_a/δ_i	Re_θ	Re_τ	$Re_{\delta 2}$	θ (mm)	H	δ (mm)	z_τ (mm)	u_τ (m s^{-1})
Double Wall	46.3	2669	453	1563	0.55	4.0	6.8	0.015	40.5

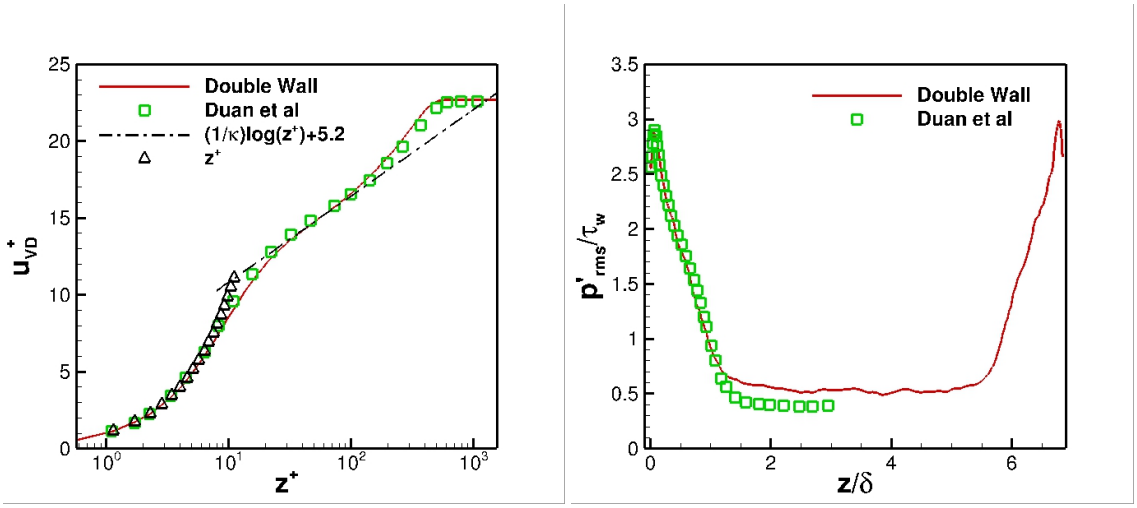

(a) (b)

Figure 4: (a) The van Driest transformed mean velocity profile; (b) wall-normal profile of r.m.s. pressure fluctuation normalized by the wall shear stress at the reference location x_a. Solid line: present Double Wall; square symbol: Duan et al [4].

III. Doak's Momentum Potential Theory

The separation of fluctuations into their acoustic, hydrodynamic (vortical) and thermal (entropic) components, in the manner of Kovasznáy [30], has proven difficult when different variables are employed for the three components. An example of this difficulty may be found in [31]. An alternative approach, Doak's MPT, circumvents these problems by choosing a single vector variable to be split into the three desired components. This section describes the application of Doak's MPT to the above-mentioned DNS database.

A. Helmholtz Decomposition

As previously stated in Section I, Doak's MPT theory involves a Helmholtz decomposition of the momentum density ($\rho\mathbf{u}$) into solenoidal and irrotational FT components as shown below,

$$\rho\mathbf{u} = \bar{\mathbf{B}} + \mathbf{B}' - \nabla\psi', \tag{2}$$

where

$$\nabla\cdot\bar{\mathbf{B}} = 0, \qquad \nabla\cdot\mathbf{B}' = 0. \tag{3}$$

Here $\bar{\mathbf{B}}$ is the mean solenoidal component, $\mathbf{B}'$ is the fluctuating solenoidal component and ψ' is the fluctuating irrotational scalar potential. Equations (2) and (3) when used with the mass conservation equation yield,

$$\nabla^2\psi' = \frac{\partial\rho'}{\partial t} \tag{4}$$

The irrotational scalar potential can be further split into acoustic and thermal FT components: $\psi' = \psi'_a + \psi'_t$, which are described by,

$$\nabla^2\psi'_a = \frac{1}{c^2}\frac{\partial p'}{\partial t}, \qquad \nabla^2\psi'_t = \frac{\partial\rho}{\partial S}\frac{\partial S'}{\partial t} \tag{5}$$

where ψ'_a and ψ'_t are the acoustic and thermal components of the irrotational momentum density, the entropy S is given by,

$$S = C_p[\log(T/T_\infty) - R\log(p/p_\infty)] \tag{6}$$

where the subscript ∞ denotes ambient values, C_p is the specific heat at constant pressure, and R is the ideal gas constant. An advantage of using Doak's MPT is that the resulting Poisson equations are derived directly from the Navier Stokes (NS) equations. As a result, MPT can be easily applied to any nonlinear problem governed by the NS equations. In the present study, MPT is employed on a 2D streamwise slice of the DNS data to study the nature of these FT components in a geometrically confined setting. A detailed analysis on the spatial structure and spectral characteristics of these FT components is presented next.

B. Fluid Thermodynamic Components

Figure 5 presents both the streamwise and wall-normal components of the hydrodynamic, acoustic and thermal FT components at an arbitrarily chosen time-step after statistical stationarity has been reached. The hydrodynamic component closely follows the development of the TBL with peaks in regions of high vorticity. As expected, these solenoidal fluctuations appear to diminish considerably away from the TBLs and towards the core of the channel as the turbulence dies out.

The acoustic component on the other hand, exhibits evidence of organized "wavepacket" structures with a high spatio-temporal coherence that develop around the strong localized vortices represented by the hydrodynamic component. This wavepacket structure is reminiscent of the classic instability wave theories that are used to model the sound generation from free shear layers [32]. Moreover, the two components of the acoustic mode are seen to represent different noise radiation mechanisms as indicated by the green arrows in Figures 5c and 5d. The streamwise component of the acoustic mode is observed to possess a highly directional downstream radiation pattern, analogous to a supersonically travelling wavy wall [33]. The wall-normal component of the acoustic mode on the other hand has a more broadband radiation pattern representative of noise radiation from decay and growth of instability waves as they move through the turbulent medium [34]. Furthermore, since the acoustic energy forms a very small part of the total boundary layer energy, the acoustic FT component is observed to be an order of magnitude lower than its hydrodynamic and thermal counterparts at the walls.

Since the thermal component is obtained from the irrotational scalar potential (ψ') in the MPT procedure, it also has a compact coherent structure but is found to be non-radiating. Although the thermal component is not observed to be an important factor in the present case, it is expected that for a high-speed flow over a cold wall, this component could reveal important insights into the unsteady heat transfer at the wall. This will pursued in the future in a separate investigation.

C. Comparison with Pressure Fluctuations

In order to obtain more insight into the structure of these FT components as a function of space and frequency, a Spectral Proper Orthogonal Decomposition (SPOD) approach is selected. Moreover, since pressure is often used as a measure of acoustic fluctuations in studies involving sound propagation from boundary layers [4], it is worthwhile to compare the structure of these FT components with pressure fluctuations. The original POD technique was first used by Lumley [35] to extract large-scale structures from turbulent flows. This POD technique is generally used in the frequency domain, and is therefore called Spectral POD (SPOD). An elaborate description of the properties of SPOD in the context of other methods can be found in [36].

Following the approach suggested by Lumley [35], the dominant structures of the flow can be determined by solving the following Fredholm integral eigenvalue problem:

$$\int R(x,x',t)\Gamma^{(n)}(x',t)dx' = \lambda^{(n)}\Gamma^{(n)}(x,t), \tag{7}$$

where R is the two-point cross correlation function and $\Gamma^{(n)}$ and $\lambda^{(n)}$ are the respective eigenfunctions and eigenvalues of the matrix R which correspond to the n^{th} POD mode. Spectral POD modes are generally computed in the frequency domain by performing a temporal Fourier transform on eq. (7) to obtain

$$\int C(x,x',\omega)\Gamma^{(n)}(x',\omega)dx' = \lambda^{(n)}(\omega)\Gamma^{(n)}(x,\omega) \tag{8}$$

where C is the cross-spectral density matrix. In order to calculate this matrix, the snapshots of the FT modes are arranged into blocks of $N_{FFT} = 512$ quantities with 50% overlap. An FFT is taken in the time domain with a periodic

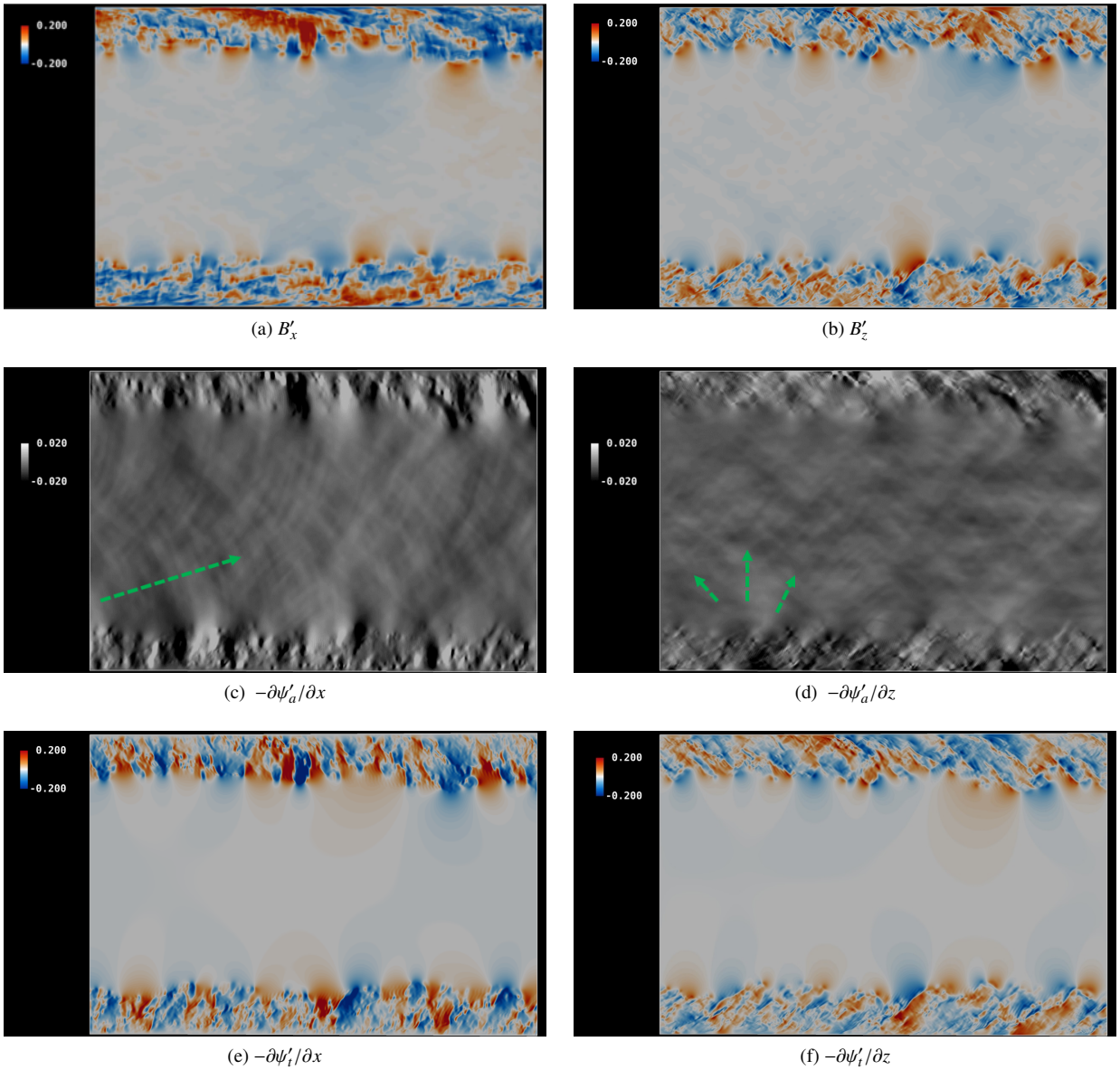

(a) B'_x (b) B'_z

(c) $-\partial\psi'_a/\partial x$ (d) $-\partial\psi'_a/\partial z$

(e) $-\partial\psi'_t/\partial x$ (f) $-\partial\psi'_t/\partial z$

Figure 5: Instantaneous snapshot of the streamwise and wall-normal FT components of $(\rho\boldsymbol{u})'$.

Hanning window to minimize spectral leakage. We have verified that the conclusions based on the general structure of the SPOD modes shown in this section are not sensitive to these choices of FFT parameters. The matrix C is calculated for each frequency by multiplying the complex FFT data with its complex conjugate. Solving the eigenvalue problem in this form yields eigenvalues and eigenfunctions that are functions of frequency.

Figure 6 shows the leading SPOD modes for p', B'_x and $-\partial\psi'_a/\partial x$ at two Strouhal numbers (St) on the bottom wall of the channel. The Strouhal Number (St) is defined as f/f_c, where f_c represents the characteristic frequency of the channel ($f_c = U_\infty/\delta_i$). It is well known that pressure fluctuations comprise of contributions from both turbulence and acoustics. The pressure signature due to the turbulent component has a convective nature (instead of a radiating one) and is often referred to as aerodynamic noise [11]. The structure of the leading SPOD pressure modes is a reflection of this behavior as evident from the distorted wavepackets due to the presence of the hydrodynamic component. Unlike the pressure wavepackets, the SPOD modes of the acoustic FT component show a more clearly distinguished wavepacket structure because the MPT procedure effectively filters out turbulent and convecting high-energy fluctuations by imposing the physical constraints of irrotationality and isentropy. Moreover, as expected, the dominant wavelength of these wavepackets decreases with an increase in frequency. The hydrodynamic SPOD modes

on the other hand, exhibit no significant coherent structures that might constitute conventional wavepackets. The initial coherence at the edge of the boundary layer is associated with the roll-up due to the interaction with the freestream and does not have a direct impact on sound radiation as the hydrodynamic mode attenuates very rapidly. Inside the boundary layer, the hydrodynamic mode structure is representative of the turbulent fluctuations induced due to the inherent shear forces in the boundary layer.

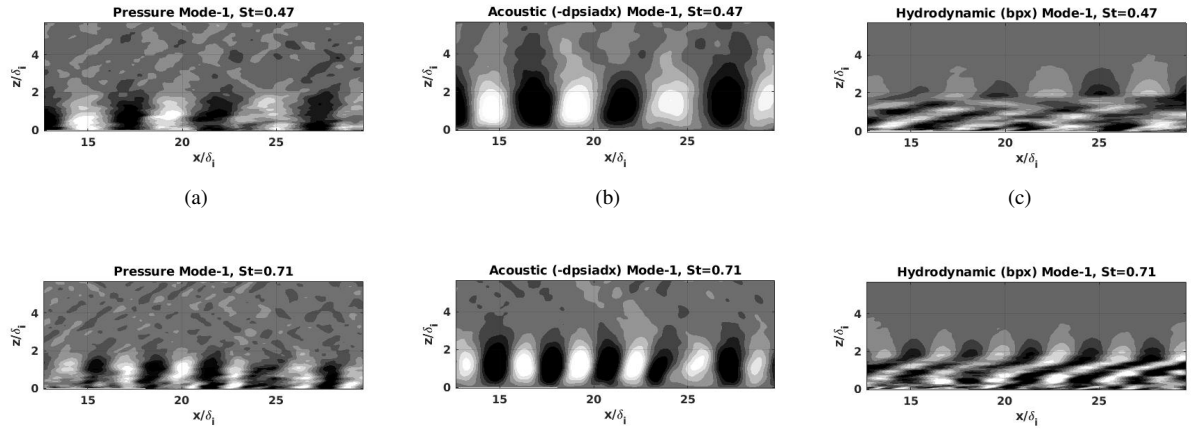

Figure 6: Leading SPOD Modes for pressure fluctuations, B'_x and $-\partial\psi_a/\partial x$.

These observations are also consistent with the total energy distribution among the SPOD modes shown in Figure 7 for each of the three variables considered. The acoustic mode displays the most skewed distribution of energy, with the leading SPOD mode contributing to more than 55% of the acoustic energy at both the frequencies. This indicates a highly coherent field as the dynamics of the acoustic component is dominated and faithfully reproduced by a few modes, making it a good candidate for reduced-order models. The hydrodynamic mode on the other hand, has the flattest distribution of percentage modal energy among its modes which is consistent with the stochastic nature of turbulence in the TBL, and the presence of convecting structures with limited spatio-temporal coherence. As expected from the previous discussion, the energy distribution for pressure SPOD modes falls between the two FT modes since the pressure field contains both coherent structures as well as random hydrodynamic fluctuations. These observations provide confidence in the effectiveness of Doak's MPT in extracting the acoustically relevant structures in the highly TBL regions at the walls of the channel.

IV. Fluctuating Stagnation Enthalpy

The previous section shows that Doak's MPT is effective at separating out the hydrodynamic, acoustic and thermal components of the channel flow as independent FT modes. Although the acoustic component does not contain any visual traces of the local mechanisms that are responsible for its origin, it can be considered as the irrotational auditory signature of turbulent structures in TBLs. This section aims to identify the local interactions in TBLs that ultimately result in noise radiation in the channel by considering the FSE of the fluid as a generalized acoustic variable.

A. FT Components of FSE

The FSE of the fluid per unit mass at any point in the flow can be written as

$$H' = h' + \frac{1}{2}\left(\frac{m_i m_i}{\rho^2}\right)', \tag{9}$$

where $h = C_v T + p/\rho$ is the static enthalpy with C_v being the specific heat at constant volume, and $m_i = \rho u_i$ is the momentum density vector. As seen in the previous section, establishing a relationship with pressure fluctuations is an important exercise in establishing the credibility of a new acoustic variable. It can be shown using simple thermodynamic relations that the FSE of the fluid at any point in the flow away from the TBLs can be expressed as

$$H' \approx \overline{c}\left[\frac{p'}{\overline{\rho c}} + \frac{\overline{u_i}}{\overline{c}}u'_i\right]. \tag{10}$$

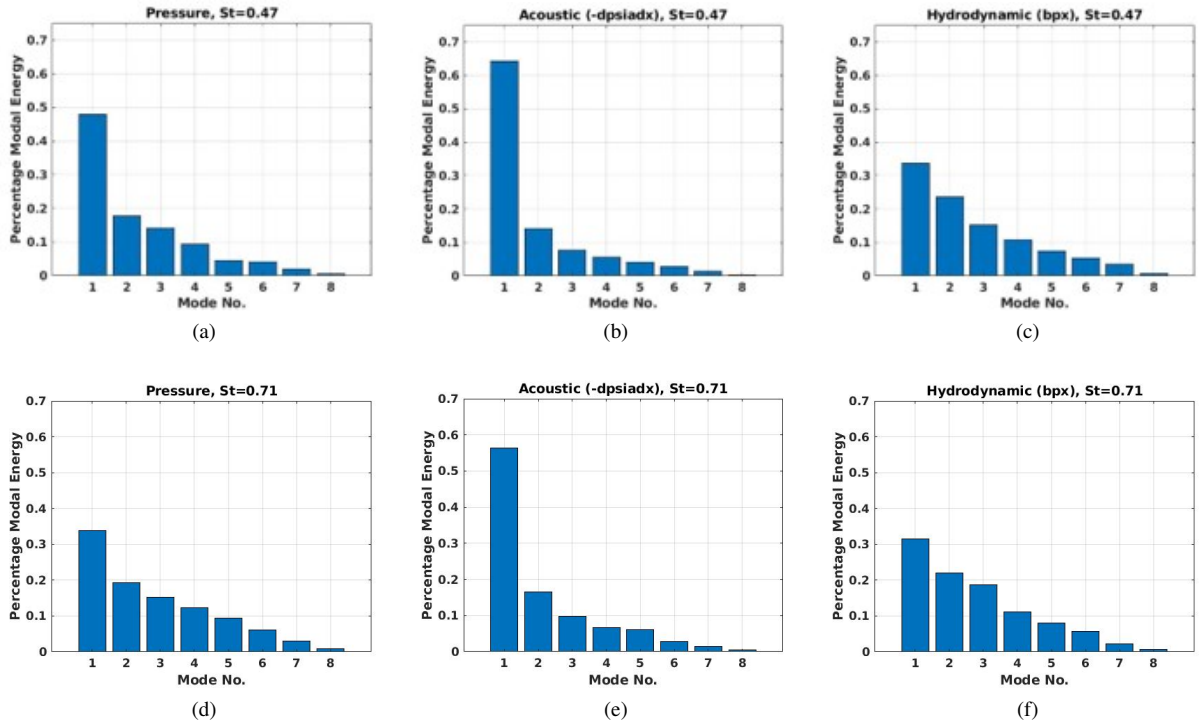

Figure 7: Distribution of Energy among SPOD modes of pressure fluctuations, B'_x and $-\partial\psi_a/\partial x$.

Figure 8 compares the scaled H' spectra with the pressure spectra at the center of the channel. The perfect overlap

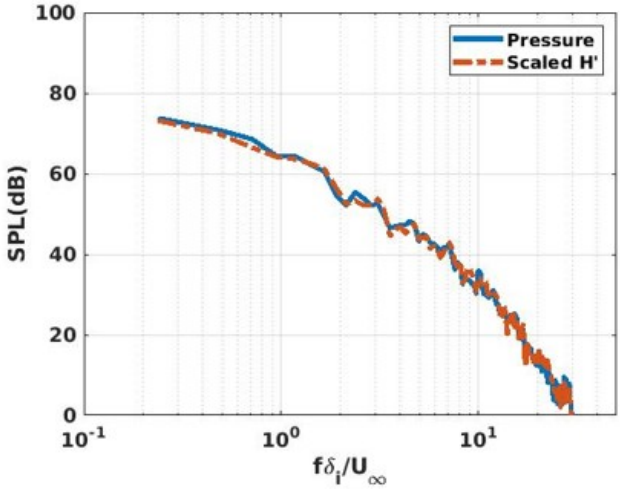

Figure 8: Spectral comparison of scaled FSE fluctuations with pressure fluctuations at three different polar angles from the jet downstream axis at $r/D = 5$.

between the two quantities away from the wall TBLs provides confidence in the use of H' and suggests that studying the sources of H' inside the TBLs can provide an improved understanding of the local mechanisms responsible for noise radiation in the channel.

However, analogous to pressure, H' also contains contributions due to both propagating and non-propagating components. In order to obtain the acoustic component of H' inside the TBLs, following Jenvey [20], H' can be further split into its hydrodynamic (H'_B), acoustic (H'_A) and thermal (H'_T) components. This is achieved by substituting eq. (2) in place of the momentum density vector in eq. (9) to obtain a linearized decomposition of H' into its FT

components as follows

$$H'_B = \left(\frac{c}{\rho}\right) \overline{\boldsymbol{M}}.\boldsymbol{B}', \tag{11}$$

$$H'_A = \left(\frac{p'}{\overline{\rho}}\right) \left(1 - \overline{\boldsymbol{M}}.\overline{\boldsymbol{M}}\right) - \left(\frac{\overline{c}}{\overline{\rho}}\right) (\overline{\boldsymbol{M}}.\nabla\psi'_a), \tag{12}$$

$$H'_T = \left(\frac{\overline{c}^2}{(\gamma-1)}\right) \left(\frac{S'}{C_p}\right) \left[1 + (\gamma-1)\overline{\boldsymbol{M}}.\overline{\boldsymbol{M}}\right], \tag{13}$$

where $\overline{\boldsymbol{M}}$ represents the mean Mach number vector. These FT components of FSE can be calculated from the DNS data as the FT components of $\rho\boldsymbol{u}$ are known from Section III.

Figure 9 shows the three FT components of H' for the channel at the same time instant as the FT components of $\rho\boldsymbol{u}$ in Figure 5. As expected, the relative shapes of the FSE FT components are consistent with those of $\rho\boldsymbol{u}$. Since H' is a scalar (unlike $\rho\boldsymbol{u}$), the radiation pattern of H'_A contains both the shallow angle and the broadband radiation patterns observed from the streamwise and wall-normal components of ψ'_a in Figure 5. Although omitted here for brevity, similar conclusions can be drawn from the SPOD modes of the FT components of FSE as in Section IIIC. This lends further credibility to the FSE analysis presented in this section.

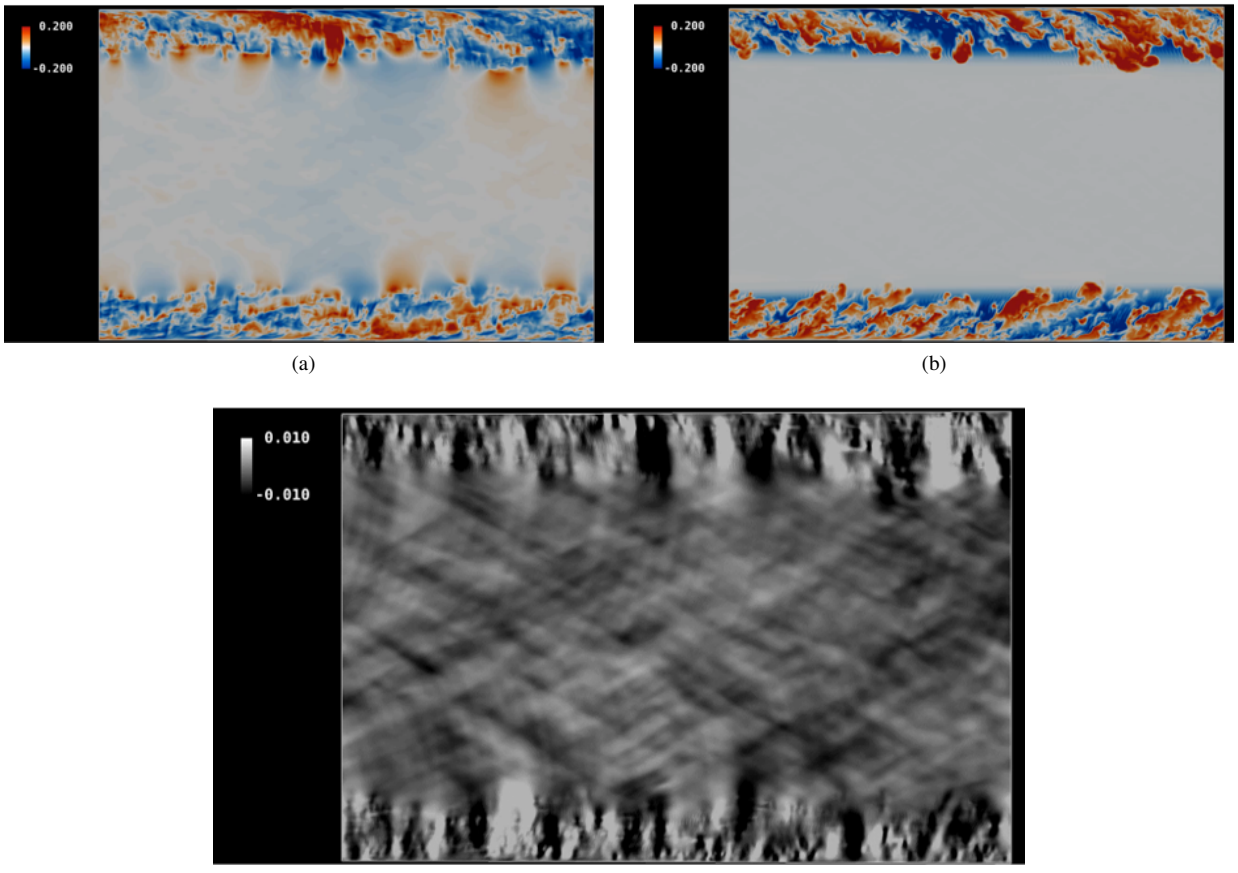

(a) (b)

(c)

Figure 9: Segregation of FSE into its FT components: (a) H'_B, (b) H'_T and (c) H'_A.

B. Convected Wave Equation

Following Doak [19], given the standard thermodynamic relations for an ideal gas, the dynamics governing the generation and propagation of H' can be obtained by recasting the NS equations in terms of H as follows

$$\frac{1}{c^2}\left\{\frac{DH}{Dt}-\frac{D}{Dt}(\frac{1}{2}u_i^2)\right\}-\frac{1}{R}\frac{DS}{Dt}+\frac{\partial u_i}{\partial x_i}=0, \tag{14}$$

$$\frac{\partial H}{\partial x_i}-\alpha_{1i}-\alpha_{2i}+\frac{\partial u_i}{\partial t}=0. \tag{15}$$

Here $D/Dt \equiv \partial/\partial t + u_k\partial/\partial x_k$ is the total derivative, $\boldsymbol{\alpha_1}$ represents the Coriolis acceleration vector and is given by

$$\alpha_{1i}=(\boldsymbol{u}\times\boldsymbol{\omega})_i, \tag{16}$$

where $\boldsymbol{\omega}$ is the vorticity vector. The term $\boldsymbol{\alpha_2}$ is a force per unit mass given by

$$\alpha_{2i}=T\frac{\partial S}{\partial x_i}+\frac{1}{\rho}\frac{\partial \tau_{ij}}{\partial x_j}+f_i, \tag{17}$$

where T is the temperature, $\boldsymbol{\tau}$ is the viscous stress tensor and f_i is the external force per unit mass (if any). By subtracting the fluctuating parts of the time derivative of eq. (14) and the divergence of eq. (15), for statistically stationary flows, the propagation and generation of H' can be written in terms of an exact, inhomogeneous, convected scalar wave equation as follows

$$\begin{aligned}\frac{\partial^2 H'}{\partial x_i^2}-\left[\frac{1}{c^2}\left\{\frac{\partial^2}{\partial t}+u_iu_j\frac{\partial^2}{\partial x_ix_j}+\left(2u_i\frac{\partial}{\partial t}-\alpha_{1i}+\alpha_{2i}-2\frac{\partial h}{\partial x_i}\right)\frac{\partial}{\partial x_i}\right\}H'\right]' = \\ \left[\left\{\frac{\partial}{\partial x_i}-\frac{1}{c^2}\left(-\alpha_{1i}+\alpha_{2i}-2\frac{\partial h}{\partial x_i}+u_iu_j\frac{\partial^2}{\partial x_ix_j}\right)\right\}([\alpha'_{1i}+\alpha'_{2i}])\right]' + \\ \left[\frac{\partial}{\partial t}\left(\frac{1}{c^2}\right)'\frac{Dh}{Dt}\right]'-\left[\frac{\partial}{\partial t}\left(\frac{1}{R}\frac{DS}{Dt}\right)'\right]'-\left[\frac{1}{c^2}u_i\frac{\partial}{\partial t}\alpha'_{2i}\right]'.\end{aligned} \tag{18}$$

The terms on the left-hand side of this equation represent the physical processes that govern the propagation of H' disturbances whereas the terms on the right-hand side represents the local mechanisms responsible for their generation. In the absence of vorticity, shear and thermal gradients, the homogeneous form of eq. (18) reduces to

$$\frac{\partial^2 H'}{\partial x_i^2}-\frac{1}{c_0^2}\left(\frac{\partial^2 H'}{\partial t^2}+2u_i\frac{\partial^2 H'}{\partial x_i\partial t}+u_iu_j\frac{\partial^2 H'}{\partial x_i\partial x_i}\right)=0, \tag{19}$$

which is a convected wave equation for the propagation of H' that includes refraction effects due to wave propagation in a moving medium. For the present case, in addition to the refraction effects, the propagation of H' is also affected by presence of vorticity, shear and thermal gradients in the TBLs at the walls. On the other hand, the sources that result in the generation of H' primarily contain the interaction of the base flow (mean and fluctuations) with the net fluctuating accelerations $\boldsymbol{\alpha'_1}$ and $\boldsymbol{\alpha'_2}$ respectively.

In order to understand the physical meaning of these acceleration terms, Figure 10 shows an instantaneous snapshot of these accelerations along for the TBL at the bottom wall. The term $\boldsymbol{\alpha'_1}$ appears in the flow due to the convection of the rotating vortices in the boundary layer. This term can therefore be interpreted as a force per unit mass representing the mixing of the flow due to the turbulence in the boundary layer. The term $\boldsymbol{\alpha'_2}$ on the other hand, consists of "streak-like" structures that represent the shear and temperature gradients due to the velocity differential in the boundary layer. As stated previously, the sources of H' involve the interaction of the base flow with these acceleration vectors. Furthermore, the terms that appear as parts of the base flow that interact with $\boldsymbol{\alpha'_1}$ and $\boldsymbol{\alpha'_2}$ to generate H' sources, also appear as propagation terms in the convection operator in the left-hand side of the equation. This implies that the sources and propagation effects are closed linked together inside the TBLs at the walls. Further investigation into this relationship will be pursued by the authors in a future separate investigation.

C. Characterization of FSE Sources

Figure 11 shows the instantaneous contours of the five most dominant source terms in eq. (18) at the bottom wall of the channel. As expected, these sources are restricted to the TBL and represent distinct mechanisms for the generation

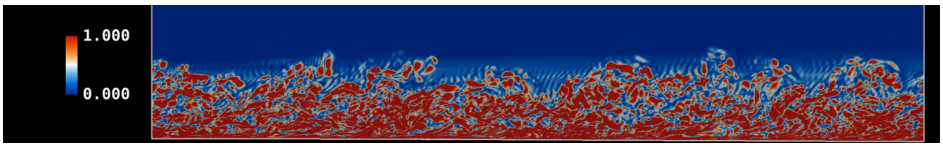

(a) $|\alpha'_1|$

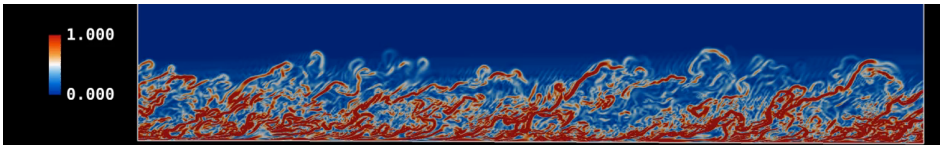

(b) $|\alpha'_2|$

Figure 10: Instantaneous magnitudes of the two types of acceleration at the bottom wall.

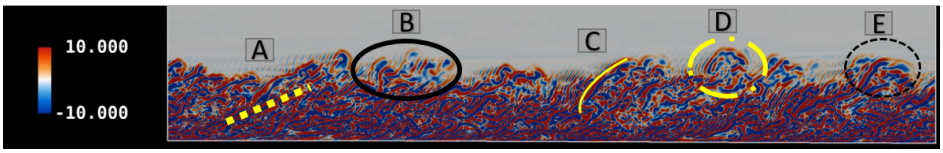

(a) $\left(\frac{\partial}{\partial x_i}(\alpha'_{1i} + \alpha'_{2i})\right)'$

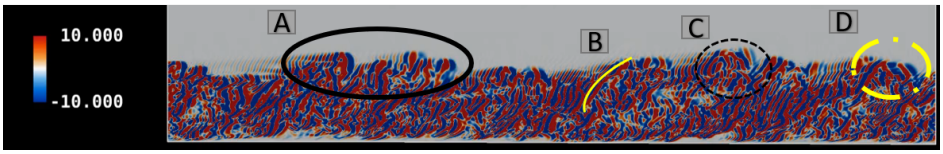

(b) $\left(-\frac{1}{c^2}\left(u_i u_j \frac{\partial^2}{\partial x_i x_j}\right)(\alpha'_{1i} + \alpha'_{2i})\right)'$

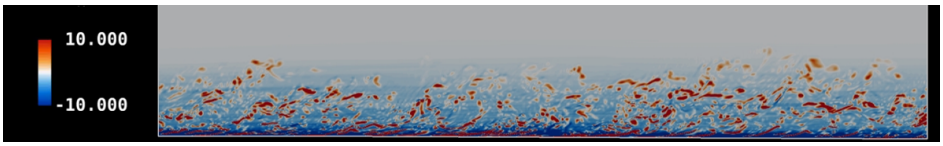

(c) $\left(-\frac{1}{c^2}(-\alpha_{1i} + \alpha_{2i})\,\alpha'_{1i}\right)'$

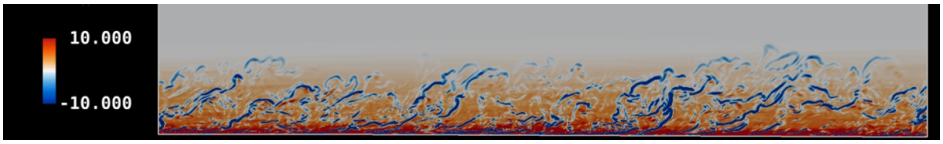

(d) $\left(-\frac{1}{c^2}(-\alpha_{1i} + \alpha_{2i})\,\alpha'_{2i}\right)'$

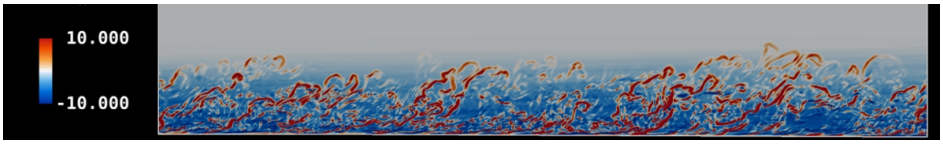

(e) $\left(\frac{2}{c^2}\frac{\partial h}{\partial x_i}(\alpha'_{1i} + \alpha'_{2i})\right)'$

Figure 11: Instantaneous contours of FSE sources in the at the bottom wall.

of H' disturbances in the TBL. Moreover, as H' contains contributions due to both propagating and non-propagating components, it is entirely possible that not all of these sources are directly related to noise radiation. It is observed that the source terms $\frac{\partial}{\partial x_i}(\alpha'_{1i} + \alpha'_{2i})$ (Figure 11a) and $-\frac{1}{c^2}\left(u_i u_j \frac{\partial^2}{\partial x_i x_j}\right)(\alpha'_{1i} + \alpha'_{2i})$ (Figure 11b) have a stochastic distribution

which suggests that these sources are related to the non-radiating components of H'. This can be observed visually by inspecting the contours of H'_B and H'_T at the bottom wall at the same time-instant as shown in Figure 12. From the

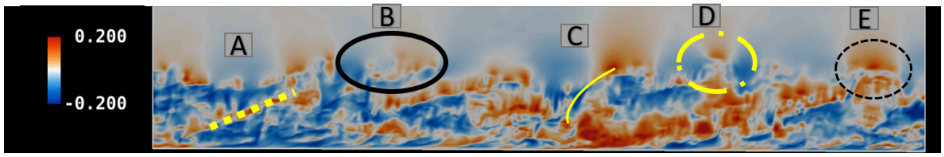

(a)

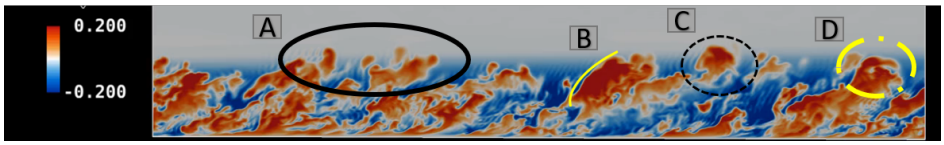

(b)

Figure 12: Instantaneous magnitudes of (a) H'_B and (b) H'_T at the bottom wall.

corresponding annotations A-E in Figures 11a and 12a and annotations A-D in Figures 11b and 12b, an exact one to one equivalence between the source $\left[\frac{\partial}{\partial x_i}(\alpha'_{1i} + \alpha'_{2i})\right]'$ and H'_B, and the source $\left[-\frac{1}{c^2}\left(u_i u_j \frac{\partial^2}{\partial x_i x_j}\right)(\alpha'_{1i} + \alpha'_{2i})\right]'$ and H'_T is observed. This indicates that these source terms are predominantly related to the production and dissipation of H'_B and H'_T in the TBL.

The term $\left[-\frac{1}{c^2}(-\alpha_{1i} + \alpha_{2i})\,\alpha'_{1i}\right]'$ on the other hand, consists of several intermittent sources distributed throughout the boundary layer which is consistent with the general intermittent nature of acoustic fluctuations, whereas, the terms $\left[-\frac{1}{c^2}(-\alpha_{1i} + \alpha_{2i})\,\alpha'_{2i}\right]'$ and $\left[\frac{2}{c^2}\frac{\partial h}{\partial x_i}(\alpha'_{1i} + \alpha'_{2i})\right]'$ contain "streaks" similar to the themal and shear gradients in $|\boldsymbol{\alpha'_2}|$ contours in Figure 10b. Furthermore, these terms represent equivalent sources and sinks in TBL from the same streaks which suggests that the combined effect of these sources in the production of H' is close to zero. These observations indicate that the interaction of the acceleration vector $\boldsymbol{\alpha'_1}$ with the base flow term $[(1/c^2)(-\boldsymbol{\alpha_1} + \boldsymbol{\alpha_2})]$ is the most acoustically relevant interaction in the TBL. A detailed investigation of this interaction is being pursued by the authors and could lead to a first-principles based understanding of the local mechanisms responsible for noise generation from supersonic TBLs. Such a study represents a first step toward understanding of the genesis of freestream disturbances in the context of actual wind-tunnel experiments and providing guidance for measuring and controlling tunnel disturbances in high-speed facilities.

V. Conclusion

A well-validated spatially evolving Mach 2.5 Double Wall DNS database is decomposed into its constituent hydrodynamic, acoustic and thermal FT components to provide insights on the nature of freestream disturbances in the confined environment of a high-speed wind tunnel. This is achieved by applying Doak's MPT in a 2D streamwise plane of an otherwise spanwise periodic DNS domain. The structure of the acoustic and hydrodynamic components is compared with pressure fluctuations using Spectral Proper Orthogonal Decomposition (SPOD). Unlike pressure fluctuations which contains contributions from both coherent structures as well as random stochastic turbulent fluctuations, the SPOD modes of the acoustic FT component exhibit a more organized wavepacket structure due to the inherent constraints imposed by the MPT procedure. This shows the effectivess of MPT in extracting these highly coherent acoustically meaningful structures hidden in the chaotic turbulent nature of the wall boundary layers of the channel. This decomposition by itself, however, is insufficient to pinpoint the precise local mechanisms responsible for the conversion of the turbulence energy into the acoustic field at the wall boundary layers. In order to identify such interactions, the Navier-Stokes equations are recast into an exact, inhomogenous convected wave equation for fluctuating stagnation enthalpy (FSE), which can also be decomposed into its hydrodynamic, thermal and acoustic components through an extension of the original MPT procedure. By a visual inspection of the spatial distribution of the FSE sources in the wave equation, it is concluded that the interaction of the Coriolis acceleration fluctuations ($\boldsymbol{\alpha'_1}$) with the base flow term $[(1/c^2)(-\boldsymbol{\alpha_1} + \boldsymbol{\alpha_2})]$ is the most acoustically relevant FSE source, where $\boldsymbol{\alpha_2}$ is a force per unit mass due to the shear and entropy gradients in the TBLs. A detailed investigation of this process is underway and will be presented in the future.

Acknowledgements

This work was performed in part under the sponsorship of the Office of Naval Research, with Dr. E. Marineau as Project Monitor. The views and conclusions contained herein are those of the authors and do not represent the opinion of the ONR.

References

[1] Laufer, J., "Some statistical properties of the pressure field radiated by a turbulent boundary layer," *The Physics of Fluids*, Vol. 7, No. 8, 1964, pp. 1191–1197.

[2] Pate, S. R. and Schueler, C., "Radiated aerodynamic noise effects on boundary-layer transition in supersonic and hypersonic wind tunnels." *AIAA Journal*, Vol. 7, No. 3, 1969, pp. 450–457.

[3] Schneider, S. P., "Effects of high-speed tunnel noise on laminar-turbulent transition," *Journal of Spacecraft and Rockets*, Vol. 38, No. 3, 2001, pp. 323–333.

[4] Duan, L., Choudhari, M. M., and Wu, M., "Numerical study of acoustic radiation due to a supersonic turbulent boundary layer," *Journal of Fluid Mechanics*, Vol. 746, 2014, pp. 165–192.

[5] Duan, L., Choudhari, M. M., and Zhang, C., "Pressure fluctuations induced by a hypersonic turbulent boundary layer," *Journal of Fluid Mechanics*, Vol. 804, 2016, pp. 578–607.

[6] Zhang, C., Duan, L., and Choudhari, M. M., "Effect of wall cooling on boundary-layer-induced pressure fluctuations at Mach 6," *Journal of Fluid Mechanics*, Vol. 822, 2017, pp. 5–30.

[7] Huang, J. and Duan, L., "Direct numerical simulation of acoustic noise generation from the nozzle wall of a hypersonic wind tunnel," AIAA Paper No. 2017-3631.

[8] Deegan, C. P., Duan, L., and Choudhari, M. M., "Direct Numerical Simulation of Acoustic Disturbances in the Rectangular Test Section of a Hypersonic Wind Tunnel," AIAA Paper No. 2018-3219.

[9] Hildebrand, N., Choudhari, M. M., and Duan, L., "Direct Numerical Simulations of Acoustic Disturbances in Various Rectangular Nozzle Configurations," AIAA Paper No. 2020-0587.

[10] Duan, L., Choudhari, M. M., Chou, A., Munoz, F., Radespiel, R., Schilden, T., Schröder, W., Marineau, E. C., Casper, K. M., Chaudhry, R. S., et al., "Characterization of freestream disturbances in conventional hypersonic wind tunnels," *Journal of Spacecraft and Rockets*, Vol. 56, No. 2, 2019, pp. 357–368.

[11] Williams, J. E. F., "Hydrodynamic noise," *Annual Review of Fluid Mechanics*, Vol. 1, No. 1, 1969, pp. 197–222.

[12] Doak, P. E., "Momentum potential theory of energy flux carried by momentum fluctuations," *Journal of Sound and Vibration*, Vol. 131, No. 1, 1989, pp. 67–90.

[13] Unnikrishnan, S. and Gaitonde, D. V., "Acoustic, hydrodynamic and thermal modes in a supersonic cold jet," *Journal of Fluid Mechanics*, Vol. 800, 2016, pp. 387–432.

[14] Unnikrishnan, S. and Gaitonde, D. V., "Transfer mechanisms from stochastic turbulence to organized acoustic radiation in a supersonic jet," *European Journal of Mechanics-B/Fluids*, Vol. 72, 2018, pp. 38–56.

[15] Unnikrishnan, S., Goparaju, K., and Gaitonde, D., "Energy-Dynamics Resulting in Turbulent and Acoustic Phenomena in an Underexpanded Jet," *Aerospace*, Vol. 5, No. 2, 2018, pp. 49.

[16] Prasad, C. and Morris, P., "Effect of fluid injection on turbulence and noise reduction of a supersonic jet," *Philosophical Transactions of the Royal Society A*, Vol. 377, No. 2159, 2019, pp. 20190082.

[17] Prasad, C. and Morris, P., "A study of noise reduction mechanisms of jets with fluid inserts," *Journal of Sound and Vibration*, 2020, pp. 115331.

[18] Unnikrishnan, S. and Gaitonde, D. V., "Kovasznay-type analysis of transition modes in a hypersonic boundary layer," AIAA Paper No. 2018-2086.

[19] Doak, P. E., "Fluctuating total enthalpy as the basic generalized acoustic field," *Theoretical and Computational Fluid Dynamics*, Vol. 10, No. 1-4, 1998, pp. 115–133.

[20] Jenvey, P. L., "The sound power from turbulence: a theory of the exchange of energy between the acoustic and non-acoustic fields," *Journal of Sound and Vibration*, Vol. 131, No. 1, 1989, pp. 37–66.

[21] Lee, J.-H. and Sung, H. J., "Structures in turbulent boundary layers subjected to adverse pressure gradients," *Journal of fluid mechanics*, Vol. 639, 2009, pp. 101–131.

[22] Kennedy, C. A. and Gruber, A., "Reduced aliasing formulations of the convective terms within the Navier–Stokes equations for a compressible fluid," *Journal of Computational Physics*, Vol. 227, No. 3, 2008, pp. 1676–1700.

[23] Pirozzoli, S., "Generalized conservative approximations of split convective derivative operators," *Journal of Computational Physics*, Vol. 229, No. 19, 2010, pp. 7180–7190.

[24] Pirozzoli, S., "Stabilized non-dissipative approximations of Euler equations in generalized curvilinear coordinates," *Journal of Computational Physics*, Vol. 230, No. 8, 2011, pp. 2997–3014.

[25] Williamson, J., "Low-storage runge-kutta schemes," *Journal of Computational Physics*, Vol. 35, No. 1, 1980, pp. 48–56.

[26] Xu, S. and Martin, M. P., "Assessment of inflow boundary conditions for compressible turbulent boundary layers," *Physics of Fluids*, Vol. 16, No. 7, 2004, pp. 2623–2639.

[27] Morgan, B., Larsson, J., Kawai, S., and Lele, S. K., "Improving low-frequency characteristics of recycling/rescaling inflow turbulence generation," *AIAA Journal*, Vol. 49, No. 3, 2011, pp. 582–597.

[28] Morgan, B., Duraisamy, K., and Lele, S. K., "Large-eddy simulations of a normal shock train in a constant-area isolator," *AIAA journal*, Vol. 52, No. 3, 2014, pp. 539–558.

[29] Thompson, K. W., "Time dependent boundary conditions for hyperbolic systems," *Journal of computational physics*, Vol. 68, No. 1, 1987, pp. 1–24.

[30] Kovasznay, L. S., "Turbulence in supersonic flow," *Journal of the Aeronautical Sciences*, Vol. 20, No. 10, 1953, pp. 657–674.

[31] Chu, B.-T. and Kovásznay, L. S., "Non-linear interactions in a viscous heat-conducting compressible gas," *Journal of Fluid Mechanics*, Vol. 3, No. 5, 1958, pp. 494–514.

[32] Tam, C. K. and Morris, P. J., "The radiation of sound by the instability waves of a compressible plane turbulent shear layer," *Journal of Fluid Mechanics*, Vol. 98, No. 2, 1980, pp. 349–381.

[33] Tam, C. K., "Mach wave radiation from high-speed jets," *AIAA Journal*, Vol. 47, No. 10, 2009, pp. 2440–2448.

[34] Jordan, P. and Colonius, T., "Wave packets and turbulent jet noise," *Annual review of fluid mechanics*, Vol. 45, 2013, pp. 173–195.

[35] Lumley, J. L., "The structure of inhomogeneous turbulent flows," *Atmospheric Turbulence and Radio Wave Propagation*, Vol. 6, 1967, pp. 166–178.

[36] Towne, A., Schmidt, O. T., and Colonius, T., "Spectral proper orthogonal decomposition and its relationship to dynamic mode decomposition and resolvent analysis," *Journal of Fluid Mechanics*, Vol. 847, 2018, pp. 821–867.